The impact of ice base topography, basal channels and subglacial discharge on basal melting — an exemplary numerical study for the floating ice tongue of the 79° North Glacier

M. Mohammadi-Aragh[1,2], K. Klingbeil[1], O. Zeising[2,3], A. Humbert[2,3], R. Timmermann[2], and H. Burchard[1]

[1]Leibniz Institute for Baltic Sea Research Warnemünde (IOW), Rostock, Germany
[2]Alfred Wegener Institute (AWI), Helmholtz Centre for Polar and Marine Research, Bremerhaven, Germany
[3]University of Bremen, Department of Geosciences, Germany

Key Points:

- Sub-km-scale channels enhance mean melt rate and spatial distribution, which can not be replicated by tuning the drag coefficient.
- Subglacial discharge regulates the melt rate in channels such that the plume dynamics' role is more critical than the heat content.
- The plume model can simulate melt patterns with great detail, which is still not possible with standard ocean models.

Corresponding author: Mahdi Mohammadi-Aragh, `mahdi.aragh@awi.de`

Abstract

Realistically approximating the basal melting of ice shelves is critical for reliable climate model projections and the process representations in ice-ocean interaction. In this regard, extensive research attributes the massive thinning of vulnerable ice shelves to basal melting enhancement driven by ocean water warming, focusing mainly on oceanic warm water intrusion into the sub-shelf basins. However, climate models mainly underestimated the impacts of probable small-scale processes at the ice-ocean interface on basal melting by using smooth ice base topographies. This paper provides new insights into how small-scale features on the ice-ocean interface contribute to the basal melting enhancement and spatial distribution. We developed a time-dependent, two-dimensional ice-shelf plume model as an optimal tool that allows a high-resolution representation of basal topography and with the unique ability to provide valuable information from the mixed boundary layer between ocean and ice shelves. In an exemplary case study for the floating ice tongue of the 79° North Glacier, systematic sensitive analyses were performed with the developed model. Our results show that the sub-km-scale basal channels with realistic dimensions increase the mean basal melt rate and generate extreme and sizeable lateral variability of melting at the grounding line. This mechanism is not reproducible with the tuning of drag coefficient. Besides, it reveals that the subglacial discharge in the channels has contradicting effects of reducing the melt rate by refreshing the sea water and increasing the freezing point while increasing the melt rate due to high water speed. However, the latter was dominant in our experiments.

Plain Language Summary

Ice shelves are floating extensions of polar ice sheets. Massive thinning of ice shelves, attributed to basal melting, influences the dynamics of outlet glaciers and, consequently climate system on a larger scale. Realistically approximating the ice shelf basal melting rate increases the reliability of process studies and climate projections. However, modelling studies on the subject have been chiefly restricted to attributing large-scale processes. In this study, in a suite of simulations, we investigated the impacts of observed narrow basal channels and subglacial discharge in developing a boundary layer flow at the ocean-ice interface, which controls basal melting. We developed a time-dependent two-dimensional plume model that, in addition to its low computational resource demands, provides valuable detailed information for basal melting. Our sensitivity analyses for the case study of the floating ice tongue of the 79° North Glacier, which experiences thinning, reveal that narrow basal channels cause both high melt rate and variability at grounding lines and elevated mean melt rate. Besides, subglacial discharge into the channels has the potential to decrease and enhance the melt rate due to refreshing the sea water and increasing the plume speed, respectively. However, for the configurations of our study, the latter was dominant.

1 Introduction

A growing body of literature recognises the importance of the basal melting of ice shelves in various fields. It is a significant area of interest in glaciology and climate studies since it modifies the buttressing of inland ice, regulates the retreats of outlet glaciers (Walker et al., 2008; Cowton et al., 2018), impacts ice discharge (Miles et al., 2022), influences the structural integrity of ice shelves (Larter, 2022) and indirectly affects sea level rise (Straneo & Heimbach, 2013; Hoffman et al., 2019; Seroussi et al., 2020; Purich, 2022). Basal melting of ice shelves also contributes to glacial meltwater, a classical problem in oceanography. Meltwater impacts sub-ice-shelf circulation (MacAyeal, 1984; Jenkins & Holland, 2002; Straneo et al., 2011; Mankoff et al., 2012) and contributes to the shelf water properties modification and enhancement of the ocean's acidification (Jacobs, 1986; Fransson et al., 2015; Bronselaer et al., 2020). On larger spatial scales, the contribution of meltwater to weakening the Atlantic meridional overturning circulation and the vulnerability of dense bottom waters are stressed (Foldvik & Gammelsrød, 1988; Böning et al., 2016; Yang et al., 2016; Williams et al., 2016). Although extensive research has been carried out, emphasizing the critical role of ice shelves basal melting, estimating the melt rate is still in its infancy. It is technically challenging due to an inadequate representation of physical processes in the models, substantial uncertainties, and limited insitu observations at ice–ocean interfaces (Thomas, 1979; Little et al., 2007; Straneo et al., 2010; Dinniman et al., 2016; Asay-Davis et al., 2017; Zeising et al., 2022). However, it is essential to better understand the hydrodynamic processes underneath ice shelves, and to constrain climate projections. This study aims to broaden our knowledge in this field by assessing the impacts of the ice base topography, basal channels, and subglacial discharge in shaping the melt rate distribution. These are the physical features whose effects are usually undervalued in climate and large-scale studies. In the rest of the introduction, we explore the obstacles and limitations in detail and explain our particular aims.

Traditionally, many studies simplify estimating basal melting by deploying smooth ice base topographies (e.g. Arzeno et al., 2014; Bernales et al., 2017; Lazeroms et al., 2018; Reese et al., 2018). In contrast, some studies recognise the crucial role of a realistic ice base topography in modelling ice shelf-ocean interaction (Holland & Feltham, 2006; Mueller et al., 2012; Wei et al., 2020). The results show a high sensitivity of spatial distribution of basal melt rate to the model geometry. In addition, the interaction of basal melting and the basal channels has long been a question of great interest (Sergienko, 2013; Drews, 2015; Watkins et al., 2021). For example, observations have suggested that sizeable lateral variability of melting is likely due to the presence of basal channels (Motyka et al., 2011). It has previously been observed that basal channels are common in Greenland (Petermann Glacier) and Antarctica (Rignot & Steffen, 2008; Le Brocq et al., 2013; Alley et al., 2016; Marsh et al., 2016; Hofstede et al., 2020; Wang et al., 2020; Humbert et al., 2021). However, studies suggested that basal channels are pronounced in regions with high basal melting (Rignot & Steffen, 2008; Wei et al., 2020). Recently, studies examined the effects of idealized, km-wide, channelized ice base topography of the floating tongue of Petermann Glacier on overall melting (Gladish et al., 2012; Sergienko, 2013; Millgate et al., 2013; Washam et al., 2019). They argue that channels protect ice shelves from strong melting. It is also suggested that such channels are the results of feedback relating to ocean induced melting and ice-shelf basal slopes (Gladish et al., 2012; Dutrieux et al., 2014). So far, however, there has been little discussion about narrow basal channels (sub-km-scale) (Dutrieux et al., 2013; Zeising, 2022). This study provides new insights into the effect of such channels on melting and highlights the importance of using a realistic ice base topography.

Recently, researchers have measured a high melt rate of about $100 - 200\,\mathrm{m\,yr^{-1}}$ at grounding lines (Shean et al., 2019; Zeising, 2022). This is of interest because it is now understood that melting at grounding lines controls the retreat of glaciers (e.g. Lilien et al., 2019; Jordan et al., 2022). The mechanisms that cause such a high melt rate are not fully understood. It is widely believed that subglacial discharge enhances the entrainment and brings heat from warm ambient water in contact with ice shelves (e.g. Jenkins, 2011; Washam et al., 2019). Nakayama et al. (2021) also draw attention to the fact that even a high-resolution regional ocean model (200 m) could not predict such a high melt rate at grounding lines unless there is subglacial discharge. However, Nakayama et al.'s modelling does not consider the role of roughness of the ice surface as well as high and narrow channels. One purpose of our study is to assess the extent to which these factors, combined with subglacial discharge, contribute to high melt rates at grounding lines. We also systematically investigate the role of subglacial discharge on the spatial distribution of melt rates.

This investigation takes the form of a case study for the 79° North Glacier (79NG), as one of the outlet glaciers of the Northeast Greenland Ice Stream, carrying alone 0.58 m sea level equivalent (Krieger et al., 2020). Recent evidence suggests that 79NG has been out of equilibrium since 2001 (Mayer et al., 2018) and that substantial thinning occurred near the grounding line (Mouginot et al., 2015; Zeising, 2022). A rapid, significant change in the basal melt rate is suggested to be the primary reason for thickness variability, with the contributions from ice flux and surface ablation being negligible (Mayer et al., 2018). A suggested explanation of the observed thinning is the increased oceanic heat flux due to the warming of Atlantic waters (Wilson & Straneo, 2015; Schaffer et al., 2017; Wilson et al., 2017; Mayer et al., 2018; Lindeman et al., 2020). It has recently been observed that a boundary current supplies warm Atlantic Intermediate Water (AIW), warmer than 1°C, to the 79NG (Schaffer et al., 2017) and its floating ice tongue (Schaffer et al., 2020). Ocean temperature rising by 0.5°C since the end of the 20th century along the existing pathway for AIW towards the 79NG (Schaffer et al., 2017) provides the potential of further increased melting at the base of the 79NG.

To date, several attempts have been made for the 79NG to estimate basal melt rates, and to map the spatial distribution of basal melting. Anhaus (2017); Mayer et al. (2018) used a one-dimensional plume model (Jenkins, 1991) to estimate basal melting along several flowlines (transects), and to investigate the sensitivity of submarine melting towards oceanic forcing. They conclude that the maximum magnitude of basal melting is reached near the grounding zone and that melt rates decay rapidly towards the calving front, which matches with in-situ radar observations from 2017 and 2018 (Zeising, 2022). Near the grounding line, Zeising (2022) found melt rates exceeding $100\,\mathrm{m\,yr^{-1}}$, while low melt rates of $< 3\,\mathrm{m\,yr^{-1}}$ were observed at the calving front. Furthermore, Wilson et al. (2017) noticed the spatial heterogeneity of basal melting inferred from high-resolution World-View satellite imagery between the years 2011 and 2015. However, there have been no systematic studies investigating spatial variability. At the same time, our knowledge about the effect of basal channels on basal melting is still very limited. We therefore designed a suite of idealized numerical experiments based on a realistic ice base topography of 79NG and general spatial characteristics of basal channels, including a synthetic network of basal channels, to estimate the basal melting and its spatial variability. Using a combination of quantitative and qualitative approaches, we perform a series of sensitivity analyses to estimate the basal melt pattern.

This study develops a two-dimensional plume model as an efficient tool for estimating basal melt rate patterns. Plume models predict the dynamics and physical properties of meltwater underneath the ice shelf that are modified by subglacial discharge and turbulent entrainment of ambient seawater (Beckmann et al., 2018; Begeman et al., 2022). The conceptual framework of a plume model is dividing the ice-ocean boundary layer into two dynamical regions (Jenkins et al., 2010), a laminar sublayer located directly at the ice-ocean interface and a turbulent mixed layer affected by rotation and stratification (Holland & Feltham, 2006; Jenkins et al., 2010; Burchard et al., 2022). In contrast to three-dimensional modelling (Losch, 2008; Timmermann et al., 2012), plume models consider the water body far from the ice base as stagnant ambient water. Nevertheless, its computational efficiency allows for a better representation of basal topography, including narrow basal channels, due to increased horizontal resolution. Therefore, it is the optimal tool for our systematic sensitivity analyses.

This paper has been divided into six sections. After this introduction, we first give a brief overview of the developed plume model and the model setup in sections 2 and 3. Section 4 investigates the impacts of ice base topography, basal channels and subglacial discharge. Discussion and conclusions are given in sections 6 and 7.

2 The plume model

2.1 Model equations

The two-dimensional plume model applied in the present study is based on time-dependent, vertically integrated prognostic equations (Holland & Feltham, 2006). This system of equations represents the buoyant turbulent gravity currents underneath large ice shelves, including basal melting at the ice-water interface and entrainment of warm, saline water at the bottom of the turbulent plume. The hydrodynamic and hydrographic properties of the plume result largely from a balance of upward buoyant forces, and turbulent fluxes at the interface between glacier ice and plume water, as well as between plume water and ambient water. Plume properties are modified by the entrainment of ambient water, i.e., changes in the mass, heat, and salt budgets. Momentum is gained from buoyancy, which is reduced by friction at the ice-water interface and entrainment. Consequently, the depth-averaged plume model consists of equations describing the conservation of mass, momentum, heat, and salt. The equations are derived assuming the turbulent, buoyant boundary layer underneath the ice shelf is vertically well mixed. The set of plume model equations derived from these principles has been comprehensively described in previous works such as Jenkins (1991), Jungclaus and Backhaus (1994), Holland and Feltham (2006), and Jenkins (2011).

The time-dependent plume thickness equation, originating from the conservation of mass under the Boussinesq approximation, reads as follows:

$$\frac{\partial h}{\partial t} + \nabla \cdot (\mathbf{u}h) = w_e + \dot{m}, \tag{1}$$

where h and $\mathbf{u} = (u, v)$ are the plume thickness and the depth-averaged horizontal velocity vector, respectively. w_e and $\dot{m}$ denote the entrainment velocity and the melt rate at the ice-water interface (see below for the parameterizations). The momentum balance of the plume is described by

$$\begin{aligned} \frac{\partial (hu)}{\partial t} + \nabla \cdot (\mathbf{u}hu) &= \frac{gh^2}{2\rho_0}\frac{\partial \rho}{\partial x} + g'h\frac{\partial (Z-h)}{\partial x} - C_d|\mathbf{u}|u + hfv, \\ \frac{\partial (hv)}{\partial t} + \nabla \cdot (\mathbf{u}hv) &= \frac{gh^2}{2\rho_0}\frac{\partial \rho}{\partial y} + g'h\frac{\partial (Z-h)}{\partial y} - C_d|\mathbf{u}|v - hfu, \end{aligned} \tag{2}$$

with the basal ice topography Z (vertical position of the ice-ocean interface), the Coriolis parameter f, the drag coefficient C_d, and the buoyancy $g' = g\Delta\rho/\rho_0$, with the gravitational acceleration g, density contrast $\Delta\rho = \rho_a - \rho$, plume density ρ, ambient density ρ_a, and reference density ρ_0. The drag coefficient C_d is either constant or calculated in agreement with the logarithmic law of the wall,

$$C_d = \max\left(0.0005\,;\left(\frac{\kappa}{\ln\frac{0.5h+z_0}{z_0}}\right)^2\right), \tag{3}$$

where $z_0 = k_s/30$ and $k_s = 0.001$ m is the characteristic height of the roughness element, with the latter chosen to yield variable drag coefficients within the range of previous studies. In our experiments, the plume density is approximated by a linear equation of state,

$$\rho = \rho_0\left[1 + \beta_s(S - S_0) - \beta_\theta(\theta - \theta_0)\right], \tag{4}$$

with absolute salinity S, potential temperature θ, haline contraction coefficient β_s, thermal expansion coefficient β_θ, reference salinity S_0, and reference potential temperature θ_0. The empirical parameters used in the present study are given in Tab. 1. The terms on the right-hand side of (2) represent baroclinic forcing (due to lateral density gradients), buoyancy, drag at the ice-water interface, and rotation, respectively.

Salinity and potential temperature of the plume are derived by vertically integrating the heat and salt budgets:

$$\frac{\partial (hS)}{\partial t} + \nabla \cdot (\mathbf{u}hS) = w_e S_a + \dot{m} S_i, \tag{5}$$

$$\frac{\partial (h\theta)}{\partial t} + \nabla \cdot (\mathbf{u}h\theta) = w_e \theta_a + \dot{m} \left[\theta_f - \frac{L_i}{c} - \frac{c_i}{c} (\theta_f - \theta_i) \right], \tag{6}$$

where subscripts a denote properties of ambient water and subscripts i denote properties of the ice, θ_f the freezing point of plume water, and θ_i core temperature of the ice shelf. Furthermore, L_i is the latent heat of fusion, c_i specific heat capacity of ice, and c specific heat capacity of sea water (values are given in Tab. 1). As defined by equations (5) and (6), salinity and temperature of the plume depend on lateral advection, entrainment of ambient water and fluxes across the ice-ocean interface. Note that the salt flux through the ice base, $\dot{m}S_i$, is negligible as $S_i = 0$.

To close the set of equations (1) – (6), parameterizations for the mass, momentum, salt and heat fluxes through the ice-ocean interface as well as through the bottom of the plume are needed. At the ice-ocean interface Z, the melt rate $\dot{m}$ and the salt and heat flux are calculated by means of a linear model. Classical approaches derive the melt rate using the balance of heat and salt flux at the ice-ocean interface (Hellmer & Olbers, 1989; Jenkins, 1991; D. M. Holland & Jenkins, 1999). In a more straightforward approach, Jenkins (2011) applied the formulation proposed by McPhee (1992) for the heat balance at the ice-ocean interface of the plume:

$$\dot{m} L_i + \dot{m} c_i (\theta_f - \theta_i) = C_d^{1/2} \Gamma_{TS} |\mathbf{u}| c (\theta - \theta_f), \tag{7}$$

with the Stanton number, $C_d^{1/2}\Gamma_{TS}$. The freezing temperature of the plume water, θ_f, is calculated by means of

$$\theta_f = \lambda_1 S + \lambda_2 + \lambda_3 Z, \tag{8}$$

with the empirical parameters λ_1, λ_2 and λ_3, see Tab. 1.

To estimate the entrainment velocity, following previous work (Jungclaus & Backhaus, 1994; Payne et al., 2007), we apply the Kochergin (1987) parameterization:

$$w_e = \frac{c_l^2}{S_m} \sqrt{|\mathbf{u}|^2 + \frac{g' h}{S_m}}, \tag{9}$$

where c_l is the Kochergin entrainment parameter, S_m is the turbulent Schmidt number (Mellor & Durbin, 1975),

$$S_m = \frac{R_i}{0.725 \left(R_i + 0.186 - \sqrt{R_i^2 - 0.316 R_i + 0.0346} \right)} \tag{10}$$

and $R_i = g'h/|\mathbf{u}|^2$ is the gradient Richardson number.

The governing equations are discretized on a staggered Arakawa C-Grid. Advection is carried out by directional-splitting, offering different options for high-order TVD limiters with reduced numerical mixing (Klingbeil et al., 2014; Mohammadi-Aragh et al., 2015). The model supports the definition of inflow boundaries, where subglacial discharge can be provided, outflow boundaries and closed boundaries, where free-slip conditions are applied.

Symbol	Value	Name	Equations
g	$9.81\,\mathrm{m\,s^{-2}}$	Gravitational acceleration	(2), (9)
κ	0.4	van Karmann constant	(3)
S_0	34.5 (g/kg)	Reference salinity	(4)
θ_0	-2.0 °C	Reference temperature	(4)
β_s	7.86×10^{-4}	Haline contraction coefficient	(4)
β_θ	$3.87 \times 10^{-5}\,\mathrm{K^{-1}}$	Thermal expansion coefficient	(4)
S_i	0 (g/kg)	Salinity of ice	(5)
c_i	$2009\,\mathrm{J\,kg^{-1}K^{-1}}$	Specific heat capacity for ice	(6), (7)
c	$3974\,\mathrm{J\,kg^{-1}K^{-1}}$	Specific heat capacity for seawater	(6), (7)
L_i	$3.35 \times 10^{5}\,\mathrm{J\,kg^{-1}}$	Latent heat of fusion for ice	(6), (7)
θ_i	-15.0 °C	Ice core temperature	(6), (7)
$C_d^{1/2}\Gamma_{TS}$	5.9×10^{-4}	Stanton number	(7)
λ_1	$-5.73 \times 10^{-2}\,°\mathrm{C}\,(\mathrm{g/kg})^{-1}$	Seawater freezing point slope	(8)
λ_2	$8.32 \times 10^{-2}\,°\mathrm{C}$	Seawater freezing point offset	(8)
λ_3	$7.61 \times 10^{-4}\,°\mathrm{C\,m^{-1}}$	Depth-dependence of freezing point	(8)
c_l	0.00125	Kochergin entrainment parameter	(9)

Table 1. Parameter settings for the model experiments. The optimal Kochergin entrainment parameter c_l was obtained by a sensitivity analysis (see Fig. 6).

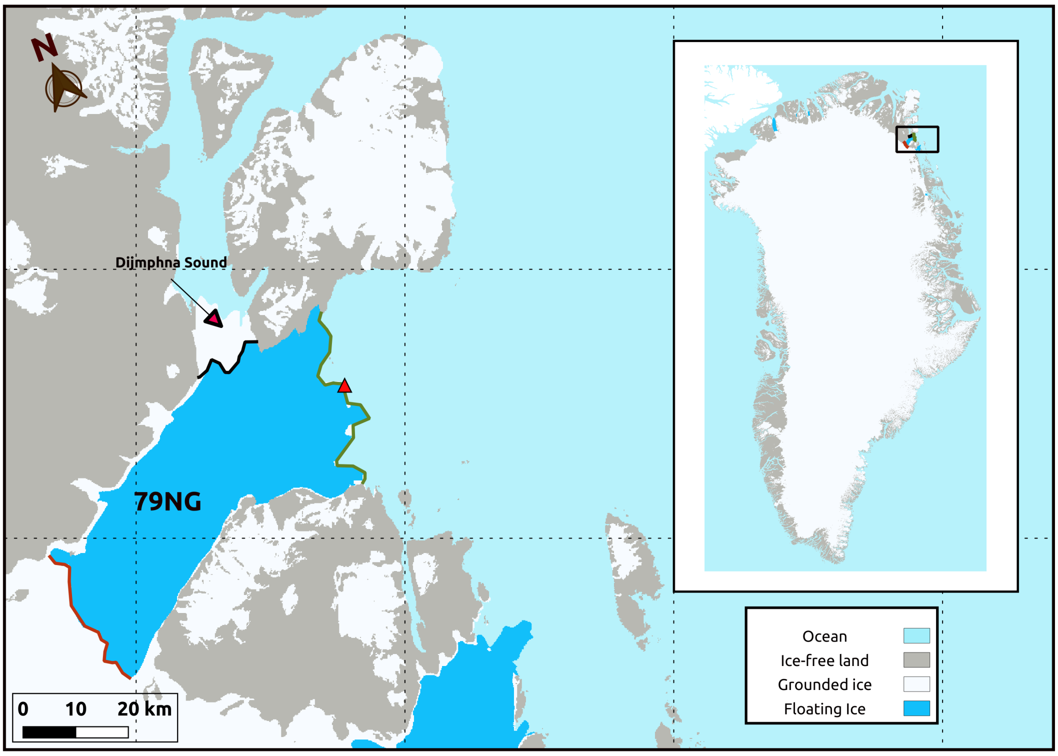

Figure 1. The location and computational domain of 79NG. The freshwater inflow cells (grounding line) are shown in red color, and the black dashed line and black simple line present outflow boundaries. The black simple line are considered as a closed boundary in our simulations. The red triangle shows the location of three CTD profiles taken in front of the main calving front at 19°56'W and 79°55'N. This figure has been produced using the BedMachine data set of the Greenland ice sheet (Morlighem et al., 2017).

3 Model setup for 79NG

3.1 Study area

The 79NG has a large floating ice tongue of approximately 70 km in length and 20 km in width that widens to around 30 km from the middle of the ice tongue towards the eastern calving front (see Fig. 1). Seismic measurements have shown a deep cavity underneath the floating tongue, with the deepest region near the mid-part of the cavity (Mayer et al., 2000). The shallowest parts of the cavity are near the calving front and at the grounding line (e.g. Mayer et al., 2000), where ice limits and narrows the inflow of water. A bottom-intensified flow carries warm AIW into the cavity over an underwater sill (Schaffer et al., 2020). Several studies based on ocean observations suggest that the residence time of AIW in the cavity is less than one year (Wilson & Straneo, 2015; Schaffer et al., 2020; Lindeman et al., 2020). A flow of warm, saline water along Dijmphna Sound (Fig. 1) towards the second, northeastern calving front of the ice tongue has not been observed (Schaffer et al., 2020; Lindeman et al., 2020), and a sill at the mouth of the fjord has assumably prohibited it (Wilson & Straneo, 2015). The mixture of AIW with subglacial discharge and meltwater generates a buoyant water mass, i.e., modified AIW, that is exported out of the cavity at a depth shallower than 250 m (Schaffer et al., 2020).

Airborne radar measurements at the 79NG from 2018 revealed a channelised basal geometry near the grounding line. While the height of narrower basal channels is roughly between 80 m to 160 m, the height of the larger channels exceeds 200 m (Zeising, 2022). The width of these channels increases from several 100 m to 1 km (sub-km-scale) along the ice flow direction. The heights of these channels decrease in the ice-flow direction.

Channels in a steady-state system are formed under constant melt rates with time leading to a positive slope in the direction of glacier termini (ice thickness thinning from upstream to downstream). When melt rates increase with time at a particular location, e.g., near the grounding line, the slope inside the channels inverts and introduces a shape like a dome. However, melt rates may increase with time in a transient system, leading to a thinner ice upstream. Airborne radar data from 2018 and the deepening of the surface above the basal channels (2016 and 2019) suggest that basal channels at the 79NG are in a transient system (Zeising, 2022).

3.2 Computational domain

The domain of interest is resolved by an equidistant grid with 150 m resolution. The computational domain for our 79NG plume model is shown in Fig. 1, which depicts computational cells (blue, floating ice), freshwater inflow cells with prescribed subglacial discharge (red, grounding line), and outflow boundaries (green, termini of ice tongue). For outflow boundaries, we avoid using zero gradients (zero-scalar-flux) boundary conditions that are typically used and are intrinsically prone to numerical instabilities. Instead, we extend the computational domain beyond the termini of the ice tongue and avoid outflow boundaries in the domain. The boundary that faces Dijmphna Sound is considered a closed boundary (yellow cells, Fig. 1) since it is characterized as grounded ice and the ice thickness and bed topography have a maximum error at this location. We also tested permitting nonzero outflow fluxes. However, the resulting magnitude and melt pattern were similar. Thus, we do not permit outflow flux in this region for the rest of this study.

3.3 Ice base topography

3.3.1 Observational data set

In Equation (2), the ice base topography determines the vertical position of the ice-ocean interface Z. We find the (raw) ice base topography (Fig. 2b) as the difference be-

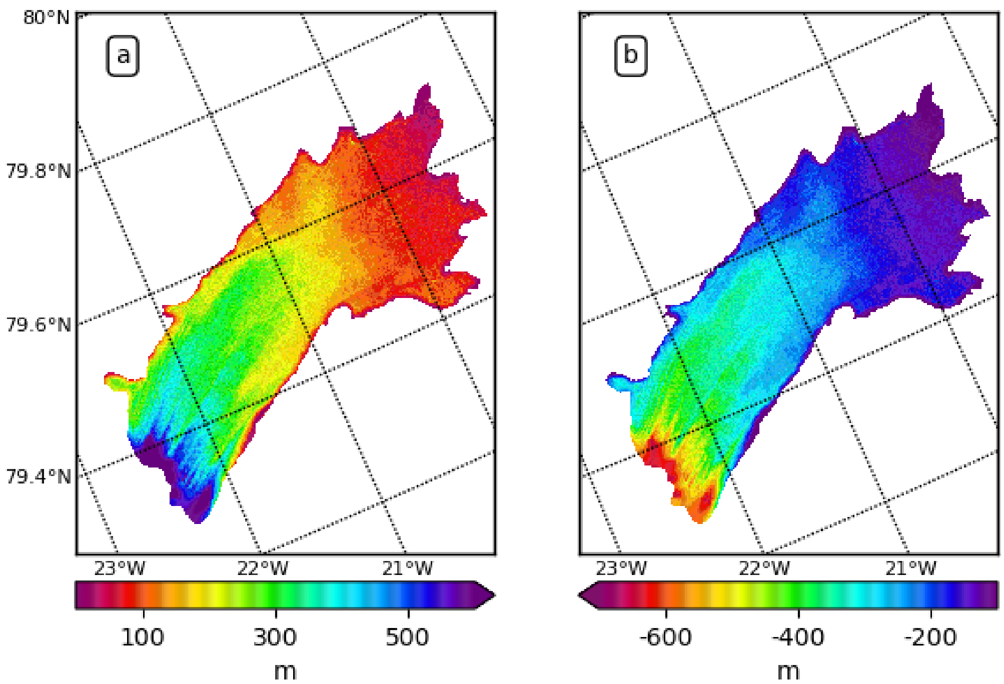

Figure 2. Maps of a) thickness of the ice tongue, and b) the raw ice base topography Z_{RAW}. This figure is produced using the BedMachine dataset of the Greenland Ice Sheet (Morlighem et al., 2017).

Table 2. Overview of different settings for the performed experiments.

Ice base topographies

Label	Z_{RAW}	Z_{RO}	—	—	—	—	—	—	—	Z_{REF}	Z_{C100S}	Z_{C200S}	Z_{C200T}
Filter (km)	—	1.35	1.65	1.95	2.25	2.55	2.85	3.15	3.45	3.75	3.75	3.75	3.75
Channels	—	—	—	—	—	—	—	—	—	—	Steady and Transient, 100 m and 200 m high		
LVT_{avg} (10^{-3})		12.2	10.0	8.7	7.7	7.0	6.5	6.0	5.6	5.3			

Subglacial discharge along grounding line

per width [$\mathrm{m}^2\ \mathrm{s}^{-1}$]	0	0.008	0.016	0.032	0.064	0.128	0.256	0.512	1.024
total [$\mathrm{m}^3\ \mathrm{s}^{-1}$]	0	224	448	896	1792	3584	7168	14336	28672

tween ice surface elevation and ice thickness (Fig. 2a) obtained from the BedMachine Greenland v3 dataset of Greenland (Morlighem et al., 2017). The dataset is produced using data from 1993 to 2016 with the nominal date of 2007. The gridded data set covers the bedrock topography and the ocean bathymetry with a horizontal grid spacing of 150 m.

Figure 2b shows that the cross-section of the ice base has an asymmetric, convex shape. The ice base's large-scale slope and thickness are reduced towards the calving fronts. The error map in Morlighem et al. (2017) indicates that the error of ice thickness and bed topography reaches a maximum near the calving front towards Dijmphna Sound. The uncertainties in ice thickness and the classification of ice as grounded or floating ice in this region are also mentioned by Schaffer et al. (2016).

3.3.2 Filtered ice base topographies

Due to the uncertainties and sharp discontinuities, we do not directly apply the raw ice base topography in our model. In order to investigate the impact of topography filtering on basal melting, we created different topographies with different filter widths for our simulations. A reference topography Z_{REF}, resembling the typical resolution of shelf sea models, was generated using a 3.75 km × 3.75 km filter. Other topographies were obtained with filter widths successively decreased by 0.3 km. The smallest applied filter width was 1.35 km × 1.35 km filter to generate the rough topography Z_{RO}.

The resulting Local Variation of Topography (LVT) is measured by

$$\mathrm{LVT}_{j,i} = \frac{1}{N_{j,i}} \sum_{n=-1}^{1} \sum_{m=-1}^{1} \left| \frac{Z\,(j,i) - Z\,(j+n, i+m)}{Z\,(j,i) + Z\,(j+n, i+m)} \right|, \tag{11}$$

where $N_{j,i}$, j,i are the number of pairs of adjacent computational cells with the central grid point, and indices of cells in both main horizontal directions of the computational coordinate, respectively. $N_{j,i}$ is maximum 8. LVT can be interpreted as the slope factor (Sikirić et al., 2009) in a one-dimensional domain. For all topographies the average LVT values are given in Tab. 2. The reference and rough topographies and their LVT maps are shown in Fig. 3.

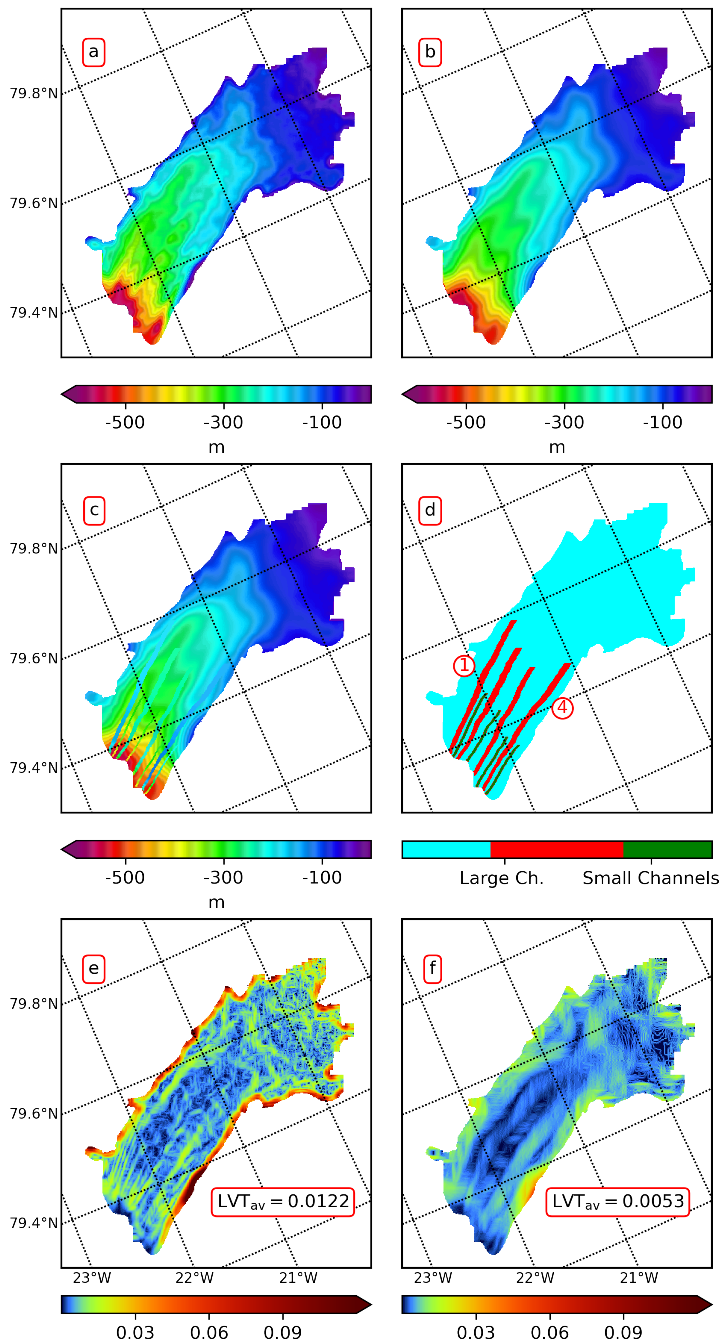

Figure 3. Comparison of ice base topographies used in the simulations and their associated local variation of topography (LVT): a) rough Z_{RO}, b) reference Z_{REF}, c) reference with transient channels Z_{C200T}, d) arrangement and geometrical characteristics of basal channels, e) LVT of Z_{RO}, f) LVT of Z_{REF}. LVT$_{\text{av}}$ denotes the average LVT of the domain.

3.3.3 Synthetic network of basal channels

The rough ice base topography indicates glacio-morphological features aligned in flow direction with a pronounced and regular structure near the grounding line. However, a network of basal channels as observed by airborne radar measurements is not present.

In order to investigate the impact of basal channels on basal melting, we added a network of large and small basal channels to the reference ice base topography. The location and arrangement of the channels are shown in Fig. 3d. We designed three topographies with different geometries for the channels. For the first two topographies, the large channels represent a steady-state system and are described by exponentially decreasing channel heights $H(x)$ with distance from the grounding line x,

$$H(x) = H_0 \exp(-b \cdot x), \tag{12}$$

with $H_0 = 100\,\mathrm{m}$ and $H_0 = 200\,\mathrm{m}$, respectively, and with $b = 0.16 \times 10^{-3}\,\mathrm{m}^{-1}$, representing an e-folding length of 6.25 km.

For the third topography the large channels represent a transient system and are described by

$$H(x) = -H_1 \exp(-b_1 x) + H_2 \exp(-b_2 x), \tag{13}$$

with $H_1 = 300\,\mathrm{m}$, $H_2 = 80\,\mathrm{m}$, $b_1 = 0.66 \times 10^{-3}\,\mathrm{m}^{-1}$, and $b_2 = 0.16 \times 10^{-3}\,\mathrm{m}^{-1}$.

For all topographies the small channels are given by (12) with $H_0 = 100\,\mathrm{m}$ and $b = 0.36 \times 10^{-3}\,\mathrm{m}^{-1}$. The profiles of all channels are shown in Fig. 4. The width of all large and small channels increases from several 100 m to 1 km along the ice flow (sub-km-scale).

We name these ice base topographies after their maximum channel heights and their stability as Z_{C200T}, Z_{C200S}, and Z_{C100S}, respectively. The ice base topography Z_{C200S} is presented in Fig. 3c.

3.4 Oceanic forcing

Ocean forcing is included in the model using the properties of the ambient water in terms of salinity, S_a, potential temperature, θ_a, and potential density, ρ_a, that determine the entrainment at the bottom of the plume as well as the reduced gravitational acceleration, g'. Here, the properties of the ambient water are considered to depend on depth only. We use Conductivity-Temperature-Depth (CTD) profiles taken from R/V Polarstern (cruise PS100) in summer 2016 (Kanzow et al., 2017) right in the pathway where warm AIW flows towards the subglacial cavity (Schaffer et al., 2020). To characterize the ambient water, we use the average of three CTD profiles taken in front of the main calving front (see Figs. 1 and 5).

3.5 Subglacial discharge

In addition to the meltwater generated by melting at the base of the floating ice tongue, which is computed as part of our plume model, we also consider a meltwater flux from subglacial discharge. Assuming the subglacial discharge to be distributed uniformly along the grounding line, we conduct experiments with different discharge rates, summarised in Tab. 2. Note that the discharge rates we prescribe are idealised and are not strictly based on theory or observations. However, Schaffer et al. (2020) suggested that for the cavity beneath the 79NG floating ice tongue, about 11% of the freshwater enters the fjord as subglacial discharge, while about 89% originate from subglacial melting at the ice-ocean interface, and we used these findings as a guideline to design a range of discharge rates. We prescribe the discharge flux per width of the grounding line, starting after a spin-up time of 5 d. We compute the total subglacial discharge (Tab. 2) by considering that the approximated length of the grounding line is 28 km.

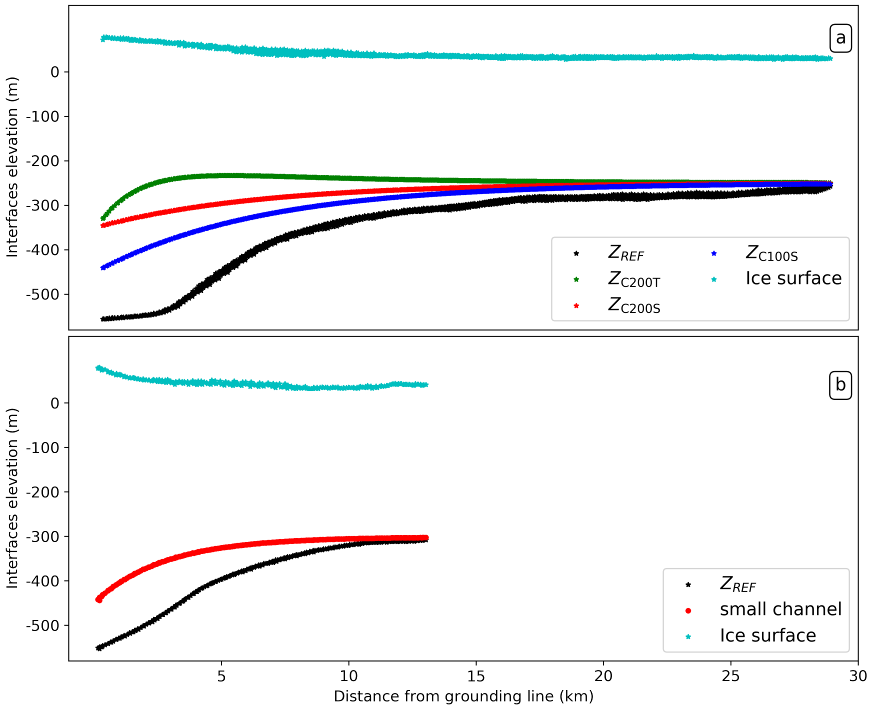

Figure 4. Comparison of ice base topographies of the synthetic channels: a) Large channels (steady and transient) and b) small channels. Both large and small channels are channel number two from Fig. 3d. Ice surface and Z_{ref} in both panels show the height and draft of the reference ice base topography along the channels.

Table 3. Names and settings of specific experiments.

Experiment	Ice base topography	Subgl. Discharge [m^3 s^{-1}]
Reference	Z_{REF}	0
Rough	Z_{RO}	0
ChannelsT	Z_{C200T}	0
RefSubD	Z_{REF}	28672
RoughSubD	Z_{RO}	28672
ChannelsTSubD	Z_{C200T}	28672
ChannelsSSubD	Z_{C200S}	28672

3.6 Model calibration

We performed sensitivity experiments on the Kochergin entrainment parameter, drag coefficient, and Local Variation of Topography (LVT). As a benchmark, we compare the simulated average basal melt rate to the mean basal melt rate estimated from remote sensing (Wilson et al., 2017). Figure 6 shows that the model is sensitive to the spatially constant drag coefficient, as the averaged basal melting decreases dramatically by increasing this coefficient. In contrast, increasing the Kochergin number increases the averaged melt rate. The Kochergin number is relevant to the heat transfer of ambient water to the plume water via the entrainment process. Accordingly, a higher Kochergin number means a higher supply of heat. Results also show that the variation of LVT affects the mean basal melt rate noticeably. Experiments with higher LVT (lower smoothness) have a higher average basal melt rate. LVT represents more physical meaning than drag coefficient since it reflects measured characteristics of ice base topography directly affecting mean melt rate.

We also investigated the sensitivity of the basal melting to different advection schemes for both momentum and tracer equations. Our results (not shown here) reveal a low sensitivity to the choice of advection schemes. We choose the MUSCL (Monotonic Upstream-centered Scheme for Conservation Laws) scheme as a diffusive advection scheme (Mohammadi-Aragh et al., 2015) for both momentum and tracer equations.

For the experiments in the following sections, we use the reference and rough ice base topographies (large green bullets in Fig. 6). We choose a constant Kochergin number of $c_l = 0.0125$ and the variable drag formulation (3).

4 Impact studies

4.1 Strategy

We perform a suite of experiments (see Tab. 3) to investigate the basal melting response to ice base topography and meltwater discharge. The experiments are configured using a combination of different ice base topographies and subglacial discharge settings given in Tab. 2.

Parameter values, initial and boundary conditions are identical for all experiments. The simulations are continued until a steady-state is reached, defined by a constant average plume thickness within the last 5 h. For the *Reference* experiment this equilibrium state is reached approximately after two days of integration. The time-averaged model results from the last 2 h are analyzed.

4.2 Impact of ice base topography

In order to investigate the impact of ice base topography, we compare the *Reference* and *Rough* simulations. The distribution of plume speed and thickness for the *Reference* simulation indicates that the plume travels mainly on two pathways along the northern and southern margins of the ice tongue (see Figs. 7a, b). A third, shorter pathway exists in the center of the ice tongue as a shallower plume with smaller water volume. This shallow plume is guided in a direction parallel to the other two streams. It merges with the plume along the southern margin in an area where the basal slope gradually flattens out. It is important to note that plume water also flows from the central pathway across the ice tongue and feeds two main southern and northern plume pathways. The lateral slope of ice base topography controls this process.

In contrast, the plume thickness in the *Rough* experiment represents a small network of narrow streams aligned in the ice stream direction (Fig. 7c). The central stream has highest plume thickness and speed. These streams have a regular, linear structure near the grounding line. For both simulations, the plume thickness increases from tens of centimeters near the grounding line to a few tens of meters towards the calving fronts. The difference in plume thickness can be explained by different local slopes of ice base topography.

A comparison of the results reveals that the complex spatial structure seen in the plume thickness of the *Rough* experiment enhances plume thickness and speed. The plume's speed for the *Rough* simulation is up by approximately 10 $\mathrm{cm\,s^{-1}}$ in a larger region compared to the *Reference* simulation. The high speed and complex spatial structure of the streams in the *Rough* simulation cause high entrainment of ambient water in the entire domain (see Fig. 8). High entrainment provides more heat for melting in case ambient water is warmer and denser than plume water.

The comparison of basal melt rate patterns and mean melt rate (Figs. 9a,b and Fig. 10) confirms higher mean melt rate for the *Rough* experiment. Besides, in multiple regions, the rate of basal melting is approximately one order of magnitude higher. Both experiments show notable consistency between the locations of patches of high entrainment and high melt rates, specifically in a region at the southern margin of the ice shelf with open-water signature, called chaos zone (Humbert et al., 2021), such as thin ice thickness (Figs. 8a,b and Fig. 9a,b). For both experiments and from Figs. 9a,b, we deduce that the spatial structure of simulated basal melting generally consists of a background of low melt rates ($< 10\,\mathrm{m\,yr^{-1}}$) and an array of wide or narrow linear features with melt rates of 40 to $60\,\mathrm{m\,yr^{-1}}$. These linear features are much more pronounced in the *Rough* simulation.

In the *Rough* simulation, the small patches of high melt rates occur entire ice shelf due to plume speed enhancement (Figs. 7b,d). However, intense melting is confined only to the deeper, strongly sloping part and along the margins of the floating ice tongue in the *Reference* simulation. Besides, comparing the spatial pattern of observational melt rates (Fig. 9d), and the results of other experiments shows a qualitative dissimilarity. Both simulations do not reproduce observed extreme melting rates at the grounding line. Most notably, the model suggests the existence of two high-melt bands along the lateral margins of the ice shelf. These high-melt bands are within the hinge zone, where the method's assumptions (Wilson et al., 2017) are not entirely applicable. Given that, it is plausible to assume that the reduced ice draft along the margins is proper due to two high-melt bands and the lateral high-melt bands are an inherent feature of the system due to the lateral slopes and the shallow ice-thickness on the sides of the ice shelf.

4.3 Impact of basal channels

In order to study the impact of basal channels, we performed the *ChannelsT* experiment (see Tab. 3) using the Z_{C200T} topography described in Section 3.3.3.

It is important to note that we do not observe horizontal circulations inside the channels since their width is smaller than the Rossby radius of deformation,

$$R_d = \frac{(g'_{\mathrm{chnl}} h_{\mathrm{chnl}})^{\frac{1}{2}}}{|f|}, \tag{14}$$

as a length scale at which Earth rotation becomes important. The $g'_{\mathrm{chnl}} = g\frac{\Delta\rho}{\rho_0}$ and h_{chnl} are the reduced gravity and the plume thickness inside the channels, respectively. Assuming a typical value of $\rho_0 = 1025\,\mathrm{kg\,m^{-3}}$, $\Delta\rho = 2\,\mathrm{kg\,m^{-3}}$, $h_{\mathrm{chnl}} = 25\,\mathrm{m}$, and the Coriolis parameter of $1.4301 \times 10^{-4}\,\mathrm{s^{-1}}$, we estimate the Rossby radius of deformation as 4.9 km which is larger than the typical width of the channels of our synthetic network (sub-km-scale).

Figure 9c shows the resulting map of melt rate. Comparison to the remote sensing based melt rates (Fig. 9d) reveals that both fields present high melt rates near the grounding line. The *ChannelsT* experiment generates an extreme melt rate $\geqslant 100\ \mathrm{m\,yr^{-1}}$ at the grounding line, even without subglacial discharge. However, the area of these extreme melt rates extends further downstream than it has been observed from remote sensing.

More details about the plume dynamics and melt rates in individual channels are presented in Sec. 5.

4.4 Impact of subglacial discharge

In order to study the impact of subglacial discharge, we performed experiments with different discharge rates given in Tab. 2.

Figure 10 compares the resulting mean basal melt rates. It shows that gradually increasing discharge enhances mean basal melting for all experiments. However, the resultant enhancement is low initially and almost invariant for the experiments configured with basal channels. These findings suggest a dependency of the mean melt rate on the type of ice base topography and subglacial discharge.

Besides, the results show that the experiments including basal channels melt ice shelves almost two to four times faster than the other experiments. From comparing the mean melt rate of experiments with different basal channel types, we conclude that transient channels cause up to 5% more melting. We also find that the type and height of channels influence the mean basal melt rate. Higher channels cause higher melting, and transient channels show highest mean melt rate. Nevertheless, these differences are minor compared to the deviation from the *Reference* experiment.

From Figure 10, it can also be seen that there is a noticeable difference between the average melt rates of the experiments configured with Z_{REF} and Z_{RO} for nearly all discharges. However, for large discharges (and in contrast to the lower discharges) the experiment configured with Z_{REF} shows a higher mean melt rate. Hence, it can be concluded that for low subglacial discharge basal channels are the main drivers of basal melting. Especially for ice base topographies without basal channels, subglacial discharge plays a prominent role in increasing the mean basal melt rate.

Figure 11 compares the spatial patterns of the melt rate for the experiments with a subglacial discharge of $28672\,\mathrm{m^3\,s^{-1}}$ and different topographies (see Tab. 3). In comparison to the experiments without subglacial discharge (Fig. 9) the areas of intense melt rates are extended. Especially, the *RefSubD* experiment shows enhance melting in comparison to corresponding *Reference* experiment without subglacial discharge. However, the *ChannelsTSubD* does not shows noticeable variability compared to *ChannelsSSubD*.

5 Plume dynamics inside the channels - Melting variability and dependency of melt rate to channels geometry

This section explores the melt pattern inside channels and the regions between them. We further investigate the adaptation of the melt pattern to freshwater subglacial discharge.

Large channels

Figs. 12a, b compare the melt rate inside all large channels from the two experiments with transient channels, *ChannelsT* and *ChannelsTSubD*, respectively, the latter with additional subglacial discharge (see Tab. 3). The results show that for all large channels, the melt rate is reduced away from the grounding line. This is in agreement with measurements by Zeising (2022). The maximum melt rate at the grounding line is about 50 to 100 $\mathrm{m\,yr^{-1}}$ for the *ChannelsT* experiment. The subglacial discharge slightly enhances the melt rate inside the large channels. For the case of no subglacial discharge we also investigated the impact of different channel types on the melt rates inside the channels. There is not a notable enhancement in melt rate in the entire channels (not shown here).

Small channels

Figure 12c shows an unexpected melt pattern for small channels in case of no subglacial discharge. For channel 4, halfway, i.e., approximately 3 to 5 km from the grounding line, the melt rate reaches a maximum value higher than 300 $\mathrm{m\,yr^{-1}}$ and then decays towards the calving front. The finding of an extreme melt rate at a short distance from the grounding line may explain the dome formation. However, caution must be taken, as the findings might not be general, and we can not extrapolate them to all channels. Nevertheless, as shown by Fig. 12d, the melt rate at the grounding line reaches 150 $\mathrm{m\,yr^{-1}}$, and the intense melting halfway weakens when subglacial discharge is released. The melt rate reduction is also surprising since we have shown so far that subglacial discharge enhances melting.

Figure 13 provides a closer assessment of channel number 4 to uncover the significance of plume water speed and water heat content in developing the two special melt rates. According to Eq. 7, we can argue that the basal melt rate is proportional to two terms representing the dynamics (speed $|\mathbf{u}|$) and the heat flux ratio ($\Delta = c(\theta - \theta_f)/[L_i + c_i\,(\theta_f - \theta_i)]$) of the plume water:

$$\dot{m} = C_d^{1/2}\Gamma_{TS}|\mathbf{u}|\Delta. \tag{15}$$

Four loci of points are shown in panels a - d of Fig.13, presenting specific geomorphological properties. Note that these interfaces are time-averaged and do not show dynamics. The space between the colored plots and black dots presents the plume thickness for both experiments. We first investigate the reason for the extreme melt rate halfway through the channel. We examine the *ChannelsT* experiment, which does not include subglacial discharge. Then, considering the *ChannelsTSubD* experiment, we investigate the reason for melt rate decay.

Figure 13a shows that the plume thickness near the grounding line with about 100 m height suddenly decreases to a few meters halfway through the channels. This sudden change in plume thickness is associated with a sudden increase in plume speed, a process opposite to the hydraulic jump that usually occurs in open channels. Besides, Fig. 13d shows no extreme heat content halfway through the channel. Therefore, a possible explanation for the extreme melt rate might be the sudden change in plume thickness and speed, which are highly related to the slope of ice base topography in the channel. It is a transition state that increases kinetic energy. In the second step, we study the second profile that includes the subglacial discharge. There is no sudden change in the plume speed profile and the interface's shape between the ambient and the plume water (Fig.13a). The subglacial discharge reduces the plume water salinity (Fig. 13b), and the entrainment increases the plume salinity in the entire water plume journey in the channel. The lower salinity at the grounding line increases the freezing point with maximum effect at the grounding line that gradually decays (Fig.13c). Therefore, the temperature above the freezing point and consequently plume water heat content is decreased at almost the entire channel (Fig.13d).

Although we expect that reducing heat content reduces the melt rate, the melt rate at the grounding line and end of channel are increased (1.3 times, Fig, 12d). Besides, heat content is slightly increased halfway, which could not cause a reduction in melt rate. Fig.12a shows that plume speed increases slightly at the grounding line and decreases 0.6 times halfway. Thus, it can be suggested that the role of dynamics of plume water in regulating melt rate (increasing at the grounding line and reducing halfway) is higher than the heat content of plume water.

Regions between the channels

Figs. 12e, f show melt rates decay generally towards the calving front. In contrast to earlier findings from (Sergienko, 2013), our results show that the melt rates in the regions between the channels are higher than inside the channels. As a shred of observational evidence, the study devoted to investigating the evolution of ice shelf melt channels at the base of the Filchner Ice Shelf presents the same results with high melt rates in the region between channels (after 25 km down to 60 km from the grounding line) and a reduction of melt rate toward calving fronts (Humbert et al., 2021). The maximum melt rate at the grounding line is about 50 to 250 $\mathrm{m\,yr^{-1}}$. Besides, the subglacial discharge noticeably enhances the melt rate in the regions between the channels and a high level of subglacial discharge.

6 Discussion

Our primary objective of this study was to assess the effects of ice base topography, basal channels, and subglacial discharge in shaping the melt rate distribution. We developed a two-dimensional plume model that provides valuable insight into the interaction of ice base topography, ambient oceanic water, and freshwater subglacial discharge, where the turbulent mixing layer transmutes its sensible heat content into phase changes. The benefits of using this model are the computational efficiency and the possibility of using a high-resolution ice base topography, including sub-km-scale basal channels. Besides, the plume model approach to solving the ice-shelf ocean boundary layer provides detailed results that are challenging for typical ocean models to replicate.

Depending on the applied ice base topography, the estimated mean melt rate ranges from 10 $\mathrm{m\,yr^{-1}}$ to 60 $\mathrm{m\,yr^{-1}}$. The broad range of mean melt rates emphasizes the fundamental role of ice base topography in predicting plume water characteristics and, consequently, the estimation of basal melting. The experiment configured using smooth ice base topography without subglacial discharge suggests the minimum mean melt rate. This finding contradicts previous studies (Gladish et al., 2012; Millgate et al., 2013), which have suggested that numerical experiments of Petermann Glacier, including basal channels, result in relatively lower melting. Our hypothesis for this discrepancy is that they have designed their experiments using km-scale channels, which are wider than the channels reported by Stewart et al. (2004).

Our results show that the experiments including the basal channels in a transient system present the highest mean melt rate for all subglacial discharges. Besides, the mean melt rate and the height of channels in a steady-state system form a direct relationship. Note that the experiments without basal channels could generate a mean melt rate with the same magnitude of channelised experiments only if substantially increased subglacial discharge is prescribed. Surprisingly, the melt rates of channelized experiments are almost invariant to low subglacial discharge. A possible explanation might be that subglacial discharge increases the mean melt rate when it brings modified discharge water in contact with a broader region, which is the case for experiments without channels.

All experiments generate maximum melt rates at the grounding line in case of availability of subglacial discharge. The similarity between the numerical and observational fields at the grounding line is highest when the ice base topography includes basal channels or a rough ice base. However, our study reveals that for the 79NG ice shelf, there are also two high-melt bands along the lateral margins of the ice shelf. An explanation might be the convex shape of the ice shelf's basal cross-section with two lateral slopes deviating warm plume water to the sides. Besides, the high-melt bands are outside the region where the observational method is entirely valid. Investigating the reason for the convex shape is beyond the aim of this study.

As mentioned in the introduction, existing ocean modeling experiments could not reproduce the recently observed extreme melt rates at grounding lines. However, they reported a strong relationship between the extreme melt rates and subglacial discharge (e.g. Nakayama et al., 2021). Although our results confirm the same link, we could replicate the extreme melt rate in experiments configured without subglacial discharge but including sub-km-scale basal channels. This finding is noteworthy since it highlights the importance of small-scale features in deriving high melt rates at the grounding lines.

Another important finding is that, in agreement with the observations, melt rates inside and outside the sub-km-scale channels decrease with distance from the grounding line. Our results suggest that melt rates outside the channels are higher than inside. Besides, subglacial discharge increases melt rate inside and outside the channels at grounding lines. One unanticipated finding, however, was estimating an extreme melt rate halfway of one small channel. This result is likely to be related to sudden, intense plume speed variation. Subsequently, subglacial discharge reduces the extreme melt rate since no sudden high plume thickness variation exists. The detailed analyses indicate that the subglacial discharge can potentially decrease the melt rate in the short channels at the grounding line by reducing the salinity of the plume water. Consequently, the freezing point increases, and the plume water heat content decreases. However, for the channel geometry and the subglacial discharge we have studied, the role of plume speed in determining the melt rate is more pronounced.

7 Conclusions

The sub-km-scale basal channels and the roughness of the ice-ocean interface are important drivers of basal melting, although the role of subglacial discharge in regulating the melt rate enhancement is significant. Large scale studies excluding the roughness of ice surface and sub-km-scale channels underestimate the mean basal melt rate and cause a systematic error in predicting the spatial melt pattern, specifically at grounding lines and ice shelf margins.

Data Availability Statement

BedMachine Greenland v3 dataset (Morlighem et al., 2017) is available at `https://nsidc.org/data/IDBMG4`. Processed CTD profiles (Kanzow et al., 2017) were downloaded from the World Data Center PANGAEA (`https://doi.org/10.1594/PANGAEA.871025`).

The model data are available at `http://doi.io-warnemuende.de/10.12754/data-2022-0007`. The two-dimensional General Ice shelf water Plume Model (GIPM) (Mohammadi-Aragh & Burchard, 2022), including instructions for compiling and running the model, can be downloaded from `https://doi.org/10.5281/zenodo.7278111`.

Acknowledgments

M.M.A., O.Z. and H.B. acknowledge the financial support by the German Federal Ministry for Education and Research (BMBF) in the framework of the GROCE project (Greenland Ice Sheet/Ocean Interaction, Grants 03F0778C and 03F0778A). K.K. and H.B. were supported by the Collaborative Research Centre TRR 181 on Energy Transfers in Atmosphere and Ocean funded by the German Research Foundation (Project 274762653). Data from airborne campaigns conducted by Alfred Wegener Institute (PRESURV79NG, PI Humbert) were used within the BedMachine dataset. We thank Sophie Nowicki, Xylar Asay-Davis, and one anonymous reviewer for their comments that improved this manuscript. We are grateful for comments by Sergey Danilov, Janin Schaffer and Martin Losch.

References

Alley, K. E., Scambos, T. A., Siegfried, M. R., & Fricker, H. A. (2016). Impacts of warm water on Antarctic ice shelf stability through basal channel formation. *Nature Geoscience*, *9*(4), 290–293.

Anhaus, P. (2017). Circulation and Ocean Driven Glacial Melting in a Greenland Fjord. *Masters dissertation, The University of Bergen*.

Arzeno, I. B., Beardsley, R. C., Limeburner, R., Owens, B., Padman, L., Springer, S. R., ... Williams, M. J. (2014). Ocean variability contributing to basal melt rate near the ice front of ross ice shelf, Antarctica. *Journal of Geophysical Research: Oceans*, *119*(7), 4214–4233.

Asay-Davis, X. S., Jourdain, N. C., & Nakayama, Y. (2017). Developments in simulating and parameterizing interactions between the Southern Ocean and the Antarctic ice sheet. *Current Climate Change Reports*, *3*(4), 316–329.

Beckmann, J., Perrette, M., & Ganopolski, A. (2018). Simple models for the simulation of submarine melt for a Greenland glacial system model. *The Cryosphere*, *12*(1), 301–323.

Begeman, C. B., Asay-Davis, X., & Van Roekel, L. (2022). Ice-shelf ocean boundary layer dynamics from large-eddy simulations. *The Cryosphere*, *16*(1), 277–295.

Bernales, J., Rogozhina, I., & Thomas, M. (2017). Melting and freezing under Antarctic ice shelves from a combination of ice-sheet modelling and observations. *Journal of Glaciology*, *63*(240), 731–744.

Böning, C. W., Behrens, E., Biastoch, A., Getzlaff, K., & Bamber, J. L. (2016). Emerging impact of Greenland meltwater on deepwater formation in the North Atlantic Ocean. *Nature Geoscience*, *9*(7), 523–527.

Bronselaer, B., Russell, J. L., Winton, M., Williams, N. L., Key, R. M., Dunne, J. P., ... Sarmiento, J. L. (2020). Importance of wind and meltwater for observed chemical and physical changes in the southern ocean. *Nature Geoscience*, *13*(1), 35–42.

Burchard, H., Bolding, K., Jenkins, A., Losch, M., Reinert, M., & Umlauf, L. (2022). The vertical structure and entrainment of subglacial melt water plumes. *Journal of Advances in Modeling Earth Systems*, *14*(3), 1–34.

Cowton, T. R., Sole, A. J., Nienow, P. W., Slater, D. A., & Christoffersen, P. (2018). Linear response of east Greenland's tidewater glaciers to ocean/atmosphere warming. *Proceedings of the National Academy of Sciences*, *115*(31), 7907–7912.

Dinniman, M. S., Asay-Davis, X. S., Galton-Fenzi, B. K., Holland, P. R., Jenkins, A., & Timmermann, R. (2016). Modeling ice shelf/ocean interaction in

Antarctica: A review. *Oceanography*, *29* (4), 144–153.
Drews, R. (2015). Evolution of ice-shelf channels in Antarctic ice shelves. *The Cryosphere*, *9* (3), 1169–1181.
Dutrieux, P., Stewart, C., Jenkins, A., Nicholls, K. W., Corr, H. F., Rignot, E., & Steffen, K. (2014). Basal terraces on melting ice shelves. *Geophysical Research Letters*, *41* (15), 5506–5513.
Dutrieux, P., Vaughan, D. G., Corr, H. F. J., Jenkins, A., Holland, P. R., Joughin, I., & Fleming, A. H. (2013). Pine island glacier ice shelf melt distributed at kilometre scales. *The Cryosphere*, *7* (5), 1543–1555.
Foldvik, A., & Gammelsrød, T. (1988). Notes on Southern Ocean hydrography, sea-ice and bottom water formation. *Palaeogeography, Palaeoclimatology, Palaeoecology*, *67* (1-2), 3–17.
Fransson, A., Chierici, M., Nomura, D., Granskog, M. A., Kristiansen, S., Martma, T., & Nehrke, G. (2015). Effect of glacial drainage water on the CO_2 system and ocean acidification state in an Arctic tidewater-glacier fjord during two contrasting years. *Journal of Geophysical Research: Oceans*, *120* (4), 2413–2429.
Gladish, C. V., Holland, D. M., Holland, P. R., & Price, S. F. (2012). Ice-shelf basal channels in a coupled ice/ocean model. *Journal of Glaciology*, *58* (212), 1227–1244.
Hellmer, H. H., & Olbers, D. J. (1989). A two-dimensional model for the thermohaline circulation under an ice shelf. *Antarctic Science*, *1* (4), 325–336.
Hoffman, M. J., Asay-Davis, X., Price, S. F., Fyke, J., & Perego, M. (2019). Effect of subshelf melt variability on sea level rise contribution from Thwaites Glacier, antarctica. *Journal of Geophysical Research: Earth Surface*, *124* (12), 2798–2822.
Hofstede, C., Beyer, S., Corr, H., Eisen, O., Hattermann, T., Helm, V., . . . others (2020). Subglacial sediment transport upstream of a basal channel in the ice shelf of Support Force Glacier (West Antarctica), identified by reflection seismics. *The Cryosphere Discussions*, 1–25.
Holland, & Feltham, D. L. (2006). The effects of rotation and ice shelf topography on frazil-laden ice shelf water plumes. *Journal of Physical Oceanography*, *36* (12), 2312–2327.
Holland, D. M., & Jenkins, A. (1999). Modeling thermodynamic ice–ocean interactions at the base of an ice shelf. *Journal of Physical Oceanography*, *29* (8), 1787–1800.
Humbert, A., Christmann, J., Corr, H. F. J., Helm, V., Höyns, L.-S., Hofstede, C., . . . Zeising, O. (2021). On the evolution of an ice shelf melt channel at the base of Filchner Ice Shelf, from observations and viscoelastic modeling. *The Cryosphere Discussions*, *2021*, 1–41.
Jacobs, S. (1986). Oceanography: Injecting ice-shelf water and air into the deep Antarctic oceans. *Nature*, *321* (6067), 196–197.
Jenkins, A. (1991). A one-dimensional model of ice shelf-ocean interaction. *Journal of Geophysical Research: Oceans*, *96* (C11), 20671–20677.
Jenkins, A. (2011). Convection-driven melting near the grounding lines of ice shelves and tidewater glaciers. *Journal of Physical Oceanography*, *41* (12), 2279–2294.
Jenkins, A., & Holland, D. M. (2002). A model study of ocean circulation beneath Filchner-Ronne Ice Shelf, Antarctica: Implications for bottom water formation. *Geophysical research letters*, *29* (8), 34–1.
Jenkins, A., Nicholls, K. W., & Corr, H. F. (2010). Observation and parameterization of ablation at the base of Ronne Ice Shelf, Antarctica. *Journal of Physical Oceanography*, *40* (10), 2298–2312.
Jordan, J. R., Gudmundsson, G. H., Jenkins, A., Stokes, C. R., Miles, B. W., & Jamieson, S. S. (2022). The sensitivity of Cook Glacier, east Antarctica, to changes in ice-shelf extent and grounding-line position. *Journal of Glaciology*,

68(269), 473–485.
Jungclaus, J. H., & Backhaus, J. O. (1994). Application of a transient reduced gravity plume model to the Denmark Strait Overflow. *Journal of Geophysical Research: Oceans*, *99*(C6), 12375–12396.
Kanzow, T., von Appen, W.-J., Schaffer, J., Köhn, E., Tsubouchi, T., Wilson, N., & Wisotzki, A. (2017). *Physical oceanography measured with CTD/Large volume Watersampler-system during POLARSTERN cruise PS100 (ARK-XXX/2)* [data set]. PANGAEA.
Klingbeil, K., Mohammadi-Aragh, M., Gräwe, U., & Burchard, H. (2014). Quantification of spurious dissipation and mixing–Discrete variance decay in a Finite-Volume framework. *Ocean Modelling*, *81*, 49–64.
Kochergin, V. (1987). Three-dimensional prognostic models. *Three-dimensional coastal ocean models*, *4*, 201–208.
Krieger, L., Floricioiu, D., & Neckel, N. (2020). Drainage basin delineation for outlet glaciers of northeast greenland based on sentinel-1 ice velocities and tandem-x elevations. *Remote Sensing of Environment*, *237*, 111483.
Larter, R. D. (2022). Basal melting, roughness and structural integrity of ice shelves. *Geophysical Research Letters*, *49*(4), e2021GL097421.
Lazeroms, W. M., Jenkins, A., Gudmundsson, G. H., & Van De Wal, R. S. (2018). Modelling present-day basal melt rates for Antarctic ice shelves using a parametrization of buoyant meltwater plumes. *The Cryosphere*, *12*(1), 49–70.
Le Brocq, A. M., Ross, N., Griggs, J. A., Bingham, R. G., Corr, H. F., Ferraccioli, F., … others (2013). Evidence from ice shelves for channelized meltwater flow beneath the Antarctic Ice Sheet. *Nature Geoscience*, *6*(11), 945–948.
Lilien, D. A., Joughin, I., Smith, B., & Gourmelen, N. (2019). Melt at grounding line controls observed and future retreat of smith, pope, and kohler glaciers. *The Cryosphere*, *13*(11), 2817–2834.
Lindeman, M. R., Straneo, F., Wilson, N. J., Toole, J. M., Krishfield, R. A., Beaird, N. L., … Schaffer, J. (2020). Ocean Circulation and Variability Beneath Nioghalvfjerdsbræ (79 North Glacier) Ice Tongue. *Journal of Geophysical Research: Oceans*, *125*(8).
Little, C. M., Oppenheimer, M., Alley, R. B., Balaji, V., Clarke, G. K., Delworth, T. L., … others (2007). Toward a new generation of ice sheet models. *Eos, Transactions American Geophysical Union*, *88*(52), 578–579.
Losch, M. (2008). Modeling ice shelf cavities in a z coordinate ocean general circulation model. *Journal of Geophysical Research: Oceans*, *113*(C8).
MacAyeal, D. R. (1984). Thermohaline circulation below the Ross Ice Shelf: A consequence of tidally induced vertical mixing and basal melting. *Journal of Geophysical Research: Oceans*, *89*(C1), 597–606.
Mankoff, K. D., Jacobs, S. S., Tulaczyk, S. M., & Stammerjohn, S. E. (2012). The role of Pine Island Glacier ice shelf basal channels in deep-water upwelling, polynyas and ocean circulation in Pine Island Bay, Antarctica. *Annals of Glaciology*, *53*(60), 123–128.
Marsh, O. J., Fricker, H. A., Siegfried, M. R., Christianson, K., Nicholls, K. W., Corr, H. F., & Catania, G. (2016). High basal melting forming a channel at the grounding line of Ross Ice Shelf, Antarctica. *Geophysical Research Letters*, *43*(1), 250–255.
Mayer, C., Reeh, N., Jung-Rothenhäusler, F., Huybrechts, P., & Oerter, H. (2000). The subglacial cavity and implied dynamics under Nioghalvfjerdsfjorden Glacier, NE-Greenland. *Geophysical Research Letters*, *27*(15), 2289–2292.
Mayer, C., Schaffer, J., Hattermann, T., Floricioiu, D., Krieger, L., Dodd, P. A., … Schannwell, C. (2018). Large ice loss variability at Nioghalvfjerdsfjorden Glacier, Northeast-Greenland. *Nature communications*, *9*(1), 1–11.
McPhee, M. G. (1992). Turbulent heat flux in the upper ocean under sea ice. *Jour-*

nal of Geophysical Research: Oceans, *97*(C4), 5365–5379.
Mellor, G., & Durbin, P. (1975). The structure and dynamics of the ocean surface mixed layer. *Journal of Physical Oceanography*, *5*(4), 718–728.
Miles, B. W., Stokes, C. R., Jamieson, S. S., Jordan, J. R., Gudmundsson, G. H., & Jenkins, A. (2022). High spatial and temporal variability in Antarctic ice discharge linked to ice shelf buttressing and bed geometry. *Scientific reports*, *12*(1), 1–14.
Millgate, T., Holland, P. R., Jenkins, A., & Johnson, H. L. (2013). The effect of basal channels on oceanic ice-shelf melting. *Journal of Geophysical Research: Oceans*, *118*(12), 6951–6964.
Mohammadi-Aragh, M., & Burchard, H. (2022). *GIPM code/setup* [Software]. Zenodo. Retrieved from `https://doi.org/10.5281/zenodo.7278111`
Mohammadi-Aragh, M., Klingbeil, K., Brüggemann, N., Eden, C., & Burchard, H. (2015). The impact of advection schemes on restratifiction due to lateral shear and baroclinic instabilities. *Ocean Modelling*, *94*, 112–127.
Morlighem, M., Williams, C. N., Rignot, E., An, L., Arndt, J. E., Bamber, J. L., … Zinglersen, K. B. (2017). BedMachine v3: Complete bed topography and ocean bathymetry mapping of Greenland from multibeam echo sounding combined with mass conservation. *Geophysical Research Letters*, *44*(21), 11–051.
Motyka, R. J., Truffer, M., Fahnestock, M., Mortensen, J., Rysgaard, S., & Howat, I. (2011). Submarine melting of the 1985 Jakobshavn Isbræ floating tongue and the triggering of the current retreat. *Journal of Geophysical Research: Earth Surface*, *116*(F1).
Mouginot, J., Rignot, E., Scheuchl, B., Fenty, I., Khazendar, A., Morlighem, M., … Paden, J. (2015). Fast retreat of Zachariæ Isstrøm, northeast Greenland. *Science*, *350*(6266), 1357–1361.
Mueller, R., Padman, L., Dinniman, M. S., Erofeeva, S., Fricker, H. A., & King, M. (2012). Impact of tide-topography interactions on basal melting of larsen C ice shelf, Antarctica. *Journal of Geophysical Research: Oceans*, *117*(C5).
Nakayama, Y., Cai, C., & Seroussi, H. (2021). Impact of subglacial freshwater discharge on pine island ice shelf. *Geophysical research letters*, *48*(18).
Payne, A. J., Holland, P. R., Shepherd, A. P., Rutt, I. C., Jenkins, A., & Joughin, I. (2007). Numerical modeling of ocean-ice interactions under Pine Island Bay's ice shelf. *Journal of Geophysical Research: Oceans*, *112*(C10).
Purich, A. (2022). How the ocean melts Antarctic ice. *Communications Earth & Environment*, *3*(1), 1–3.
Reese, R., Albrecht, T., Mengel, M., Asay-Davis, X., & Winkelmann, R. (2018). Antarctic sub-shelf melt rates via pico. *The Cryosphere*, *12*(6), 1969–1985.
Rignot, E., & Steffen, K. (2008). Channelized bottom melting and stability of floating ice shelves. *Geophysical Research Letters*, *35*(2).
Schaffer, J., Kanzow, T., von Appen, W.-J., von Albedyll, L., Arndt, J. E., & Roberts, D. H. (2020). Bathymetry constrains ocean heat supply to Greenland's largest glacier tongue. *Nature Geoscience*, *13*(3), 227–231.
Schaffer, J., Timmermann, R., Arndt, J. E., Kristensen, S. S., Mayer, C., Morlighem, M., & Steinhage, D. (2016). A global, high-resolution data set of ice sheet topography, cavity geometry, and ocean bathymetry. *Earth System Science Data*, *8*(2), 543–557.
Schaffer, J., von Appen, W.-J., Dodd, P. A., Hofstede, C., Mayer, C., de Steur, L., & Kanzow, T. (2017). Warm water pathways toward Nioghalvfjerdsfjorden Glacier, Northeast Greenland. *Journal of Geophysical Research: Oceans*, *122*(5), 4004–4020.
Sergienko, O. (2013). Basal channels on ice shelves. *Journal of Geophysical Research: Earth Surface*, *118*(3), 1342–1355.
Seroussi, H., Nowicki, S., Payne, A. J., Goelzer, H., Lipscomb, W. H., Abe-Ouchi, A., … others (2020). ISMIP6 Antarctica: a multi-model ensemble of the

Antarctic ice sheet evolution over the 21st century. *The Cryosphere*, *14*(9), 3033–3070.

Shean, D. E., Joughin, I. R., Dutrieux, P., Smith, B. E., & Berthier, E. (2019). Ice shelf basal melt rates from a high-resolution digital elevation model (dem) record for pine island glacier, Antarctica. *The Cryosphere*, *13*(10), 2633–2656.

Sikirić, M. D., Janeković, I., & Kuzmić, M. (2009). A new approach to bathymetry smoothing in sigma-coordinate ocean models. *Ocean Modelling*, *29*(2), 128–136.

Stewart, C., Rignot, E., Steffen, K., Cullen, N., & Ruff, R. (2004). Basal topography and thinning rates of Petermann Gletscher, northern Greenland, measured by ground-based phase-sensitive radar. *Res., Bergen, Norway*.

Straneo, F., Curry, R. G., Sutherland, D. A., Hamilton, G. S., Cenedese, C., Våge, K., & Stearns, L. A. (2011). Impact of fjord dynamics and glacial runoff on the circulation near Helheim Glacier. *Nature Geoscience*, *4*(5), 322–327.

Straneo, F., Hamilton, G. S., Sutherland, D. A., Stearns, L. A., Davidson, F., Hammill, M. O., … Rosing-Asvid, A. (2010). Rapid circulation of warm subtropical waters in a major glacial fjord in East Greenland. *Nature Geoscience*, *3*(3), 182–186.

Straneo, F., & Heimbach, P. (2013). North Atlantic warming and the retreat of Greenland's outlet glaciers. *Nature*, *504*(7478), 36–43.

Thomas, R. H. (1979). Ice shelves: a review. *Journal of Glaciology*, *24*(90), 273–286.

Timmermann, R., Wang, Q., & Hellmer, H. (2012). Ice-shelf basal melting in a global finite-element sea-ice/ice-shelf/ocean model. *Annals of Glaciology*, *53*(60), 303–314.

Walker, R., Dupont, T., Parizek, B., & Alley, R. (2008). Effects of basal-melting distribution on the retreat of ice-shelf grounding lines. *Geophysical research letters*, *35*(17).

Wang, Z., Song, X., Zhang, B., Liu, T., & Geng, H. (2020). Basal Channel Extraction and Variation Analysis of Nioghalvfjerdsfjorden Ice Shelf in Greenland. *Remote Sensing*, *12*(9), 1474.

Washam, P., Nicholls, K. W., Münchow, A., & Padman, L. (2019). Summer surface melt thins petermann gletscher ice shelf by enhancing channelized basal melt. *Journal of Glaciology*, *65*(252), 662–674.

Watkins, R. H., Bassis, J. N., & Thouless, M. (2021). Roughness of ice shelves is correlated with basal melt rates. *Geophysical Research Letters*, *48*(21), e2021GL094743.

Wei, W., Blankenship, D. D., Greenbaum, J. S., Gourmelen, N., Dow, C. F., Richter, T. G., … others (2020). Getz ice shelf melt enhanced by freshwater discharge from beneath the west Antarctic Ice Sheet. *The Cryosphere*, *14*(4), 1399–1408.

Williams, G., Herraiz-Borreguero, L., Roquet, F., Tamura, T., Ohshima, K., Fukamachi, Y., … others (2016). The suppression of Antarctic bottom water formation by melting ice shelves in Prydz Bay. *Nature Communications*, *7*(1), 1–9.

Wilson, N., & Straneo, F. (2015). Water exchange between the continental shelf and the cavity beneath Nioghalvfjerdsbræ (79 North Glacier). *Geophysical Research Letters*, *42*(18), 7648–7654.

Wilson, N., Straneo, F., & Heimbach, P. (2017). Satellite-derived submarine melt rates and mass balance (2011-2015) for Greenland's largest remaining ice tongues. *Cryosphere*, *11*(6).

Yang, Q., Dixon, T. H., Myers, P. G., Bonin, J., Chambers, D., Van Den Broeke, M., … Mortensen, J. (2016). Recent increases in Arctic freshwater flux affects Labrador Sea convection and Atlantic overturning circulation. *Nature communications*, *7*(1), 1–8.

Zeising, O. (2022). Glaciological observations using phase-sensitive radar. *Doctoral dissertation, Universität Bremen*.

Zeising, O., Steinhage, D., Nicholls, K. W., Corr, H. F., Stewart, C. L., & Humbert, A. (2022). Basal melt of the southern Filchner Ice Shelf, Antarctica. *The Cryosphere*, *16*(4), 1469–1482.

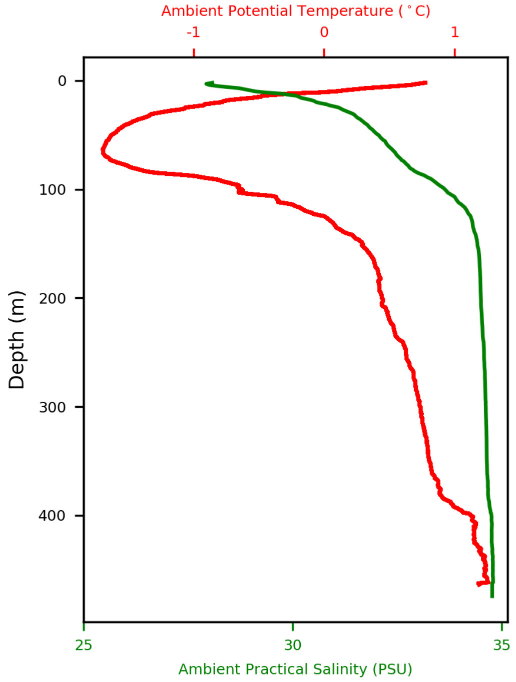

Figure 5. Temperature (red) and salinity (green) profiles as averages over three CTD casts (Kanzow et al., 2017) taken in front of the main (eastern) calving front of the floating ice tongue (see Fig. 1).

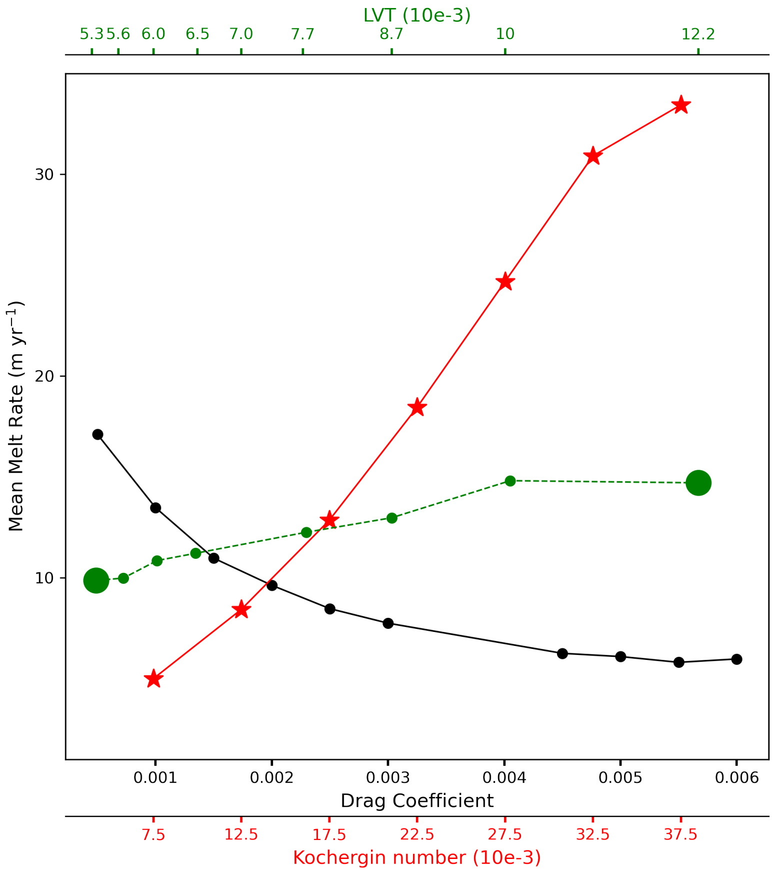

Figure 6. Effect of constant drag coefficient (black), Kochergin entrainment parameter (red), and smoothness of ice topography (green) on the estimated spatially averaged melt rate. Solid lines represent simulations with Z_{REF} ice base topography and a constant drag coefficient (C_d=2.5 × 10^{-3} for the simulations with a varying Kochergin parameter) and the dashed line represent simulations with a variable drag coefficient according to (3). Circle marker points represent simulations with a constant Kochergin entrainment parameter (c_l = 0.0275). The settings marked by the large green circle markers with measured smoothness (LVT) of 5.3 × 10^{-3} and 12.2 × 10^{-3} indicate the *Reference* and *Rough* simulations used to study the impact of ice base topographies.

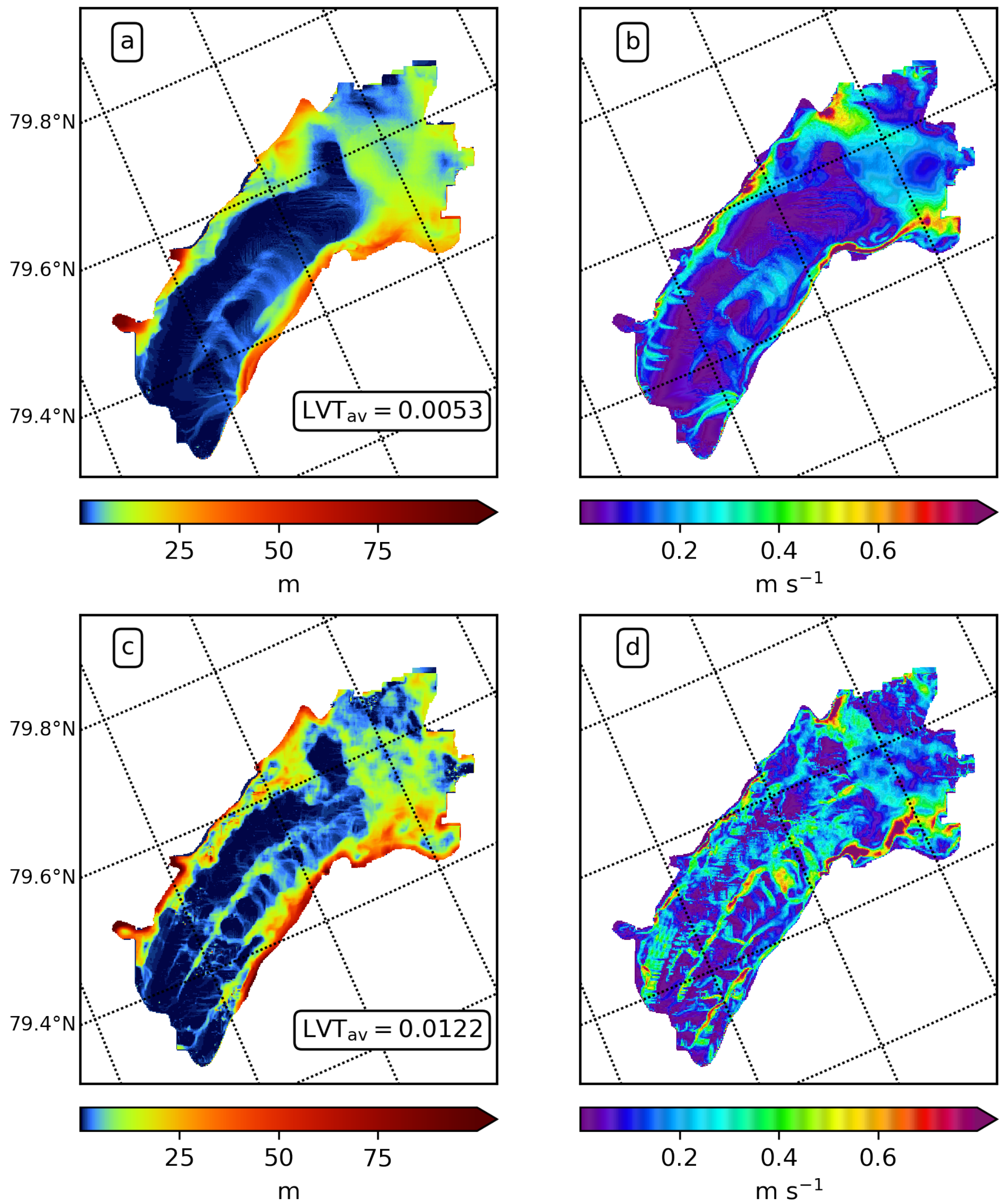

Figure 7. Results from the *Reference* experiment a) plume thickness, b) plume speed, and the *Rough* experiment c) plume thickness, and d) plume speed.

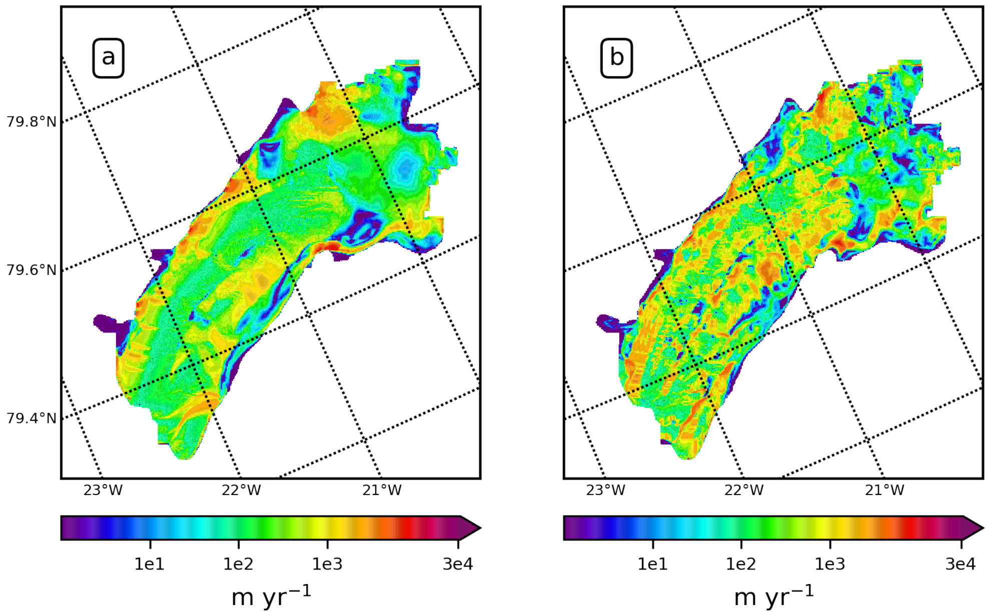

Figure 8. Entrainment rate in the a) *Reference*, and b) *Rough* experiments. Note the logarithmic color scale.

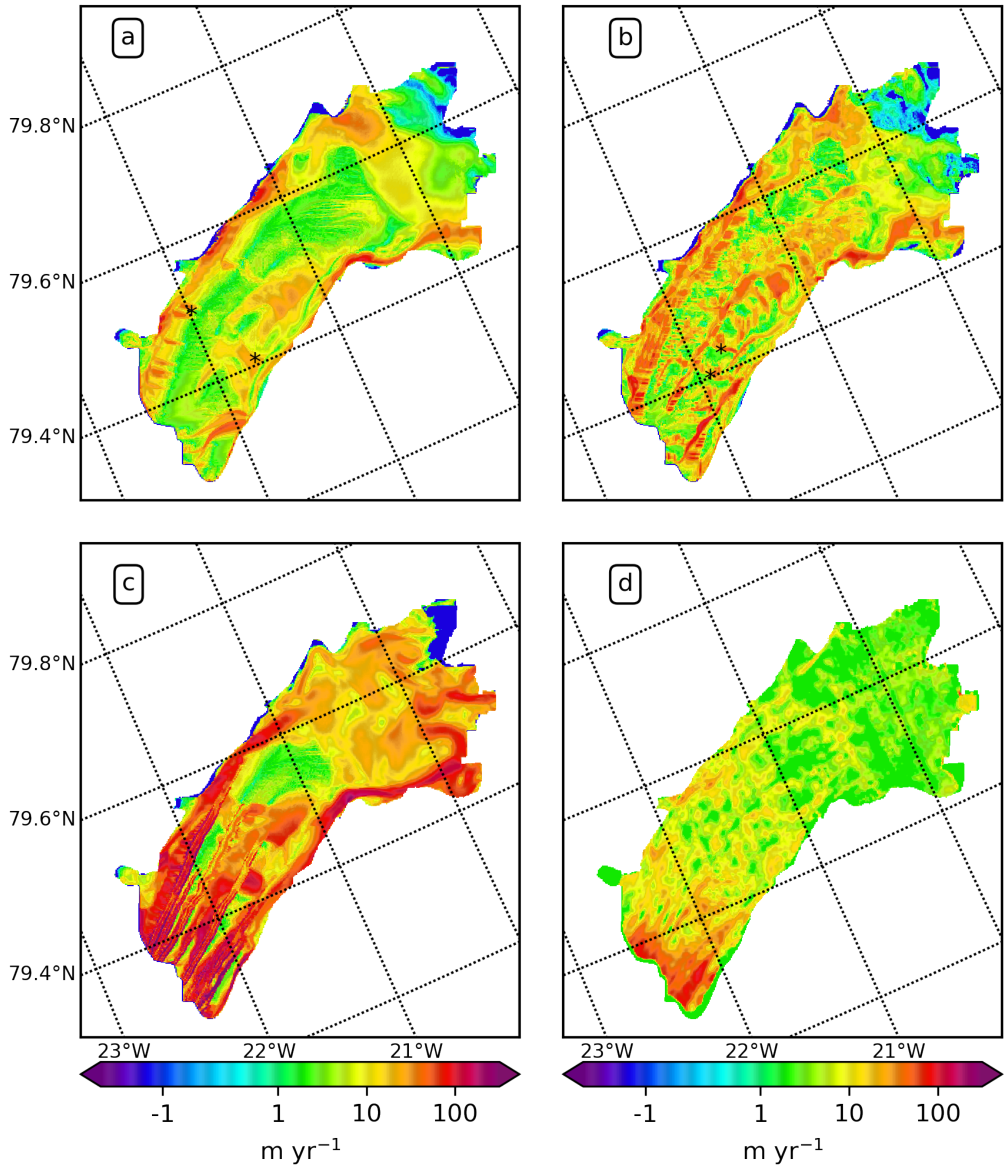

Figure 9. Basal melt rate in the a) *Reference* experiment using the smooth ice base topography (Z_{REF}), b) *Rough* experiment using the rough ice base topography (Z_{RO}), c) *ChannelsT* experiment using Z_{C200S} synthetic ice base topography and d) observation (Wilson et al., 2017). Note the logarithmic color scale. The black stars in panels a and b indicate four examples of linear features observed in melt pattern.

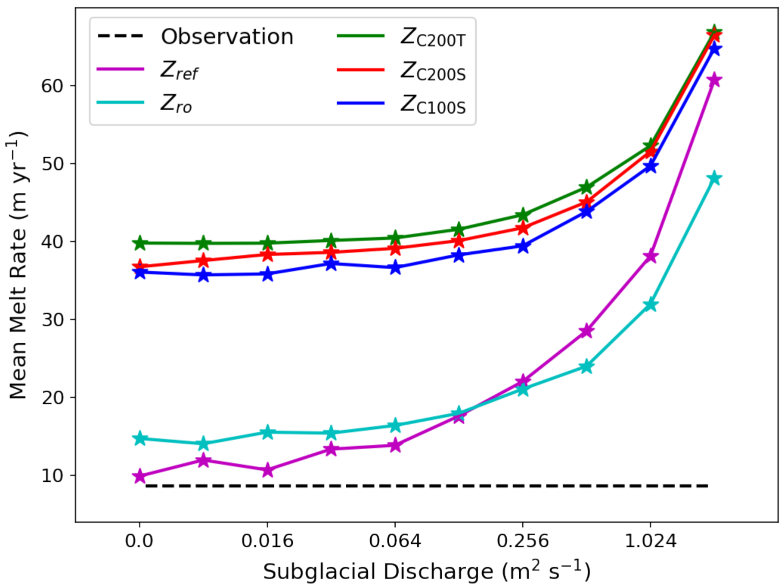

Figure 10. Area-averaged basal melt rate of the floating ice tongue for simulations with different ice base topographies and different subglacial discharges. The dashed black line indicates the observational melt rate estimate by (Wilson et al., 2017) for unknown subglacial discharge.

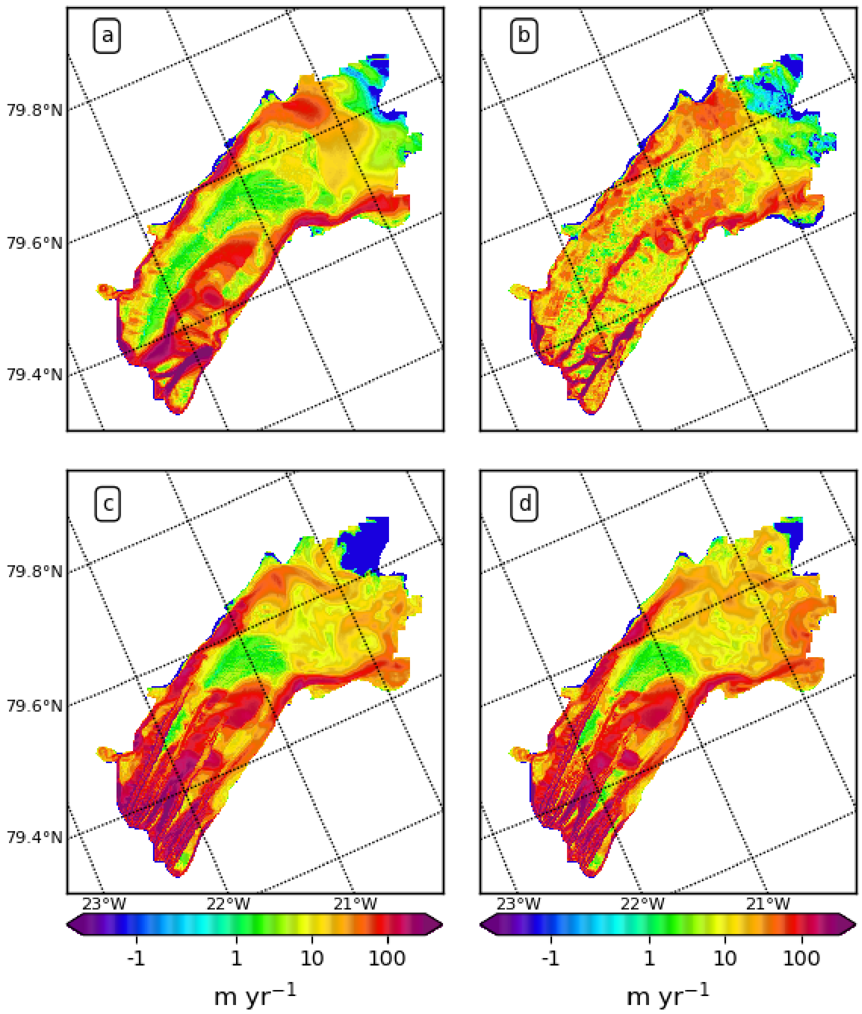

Figure 11. Maps of basal melt rates for the different experiments considering subglacial discharge (28672 $m^3\,s^{-1}$): a) *RefSubD*, b) *RoughSubD*, c) *ChannelsTSubD*, and d) *ChannelsSSubD*. Note the logarithmic color scale.

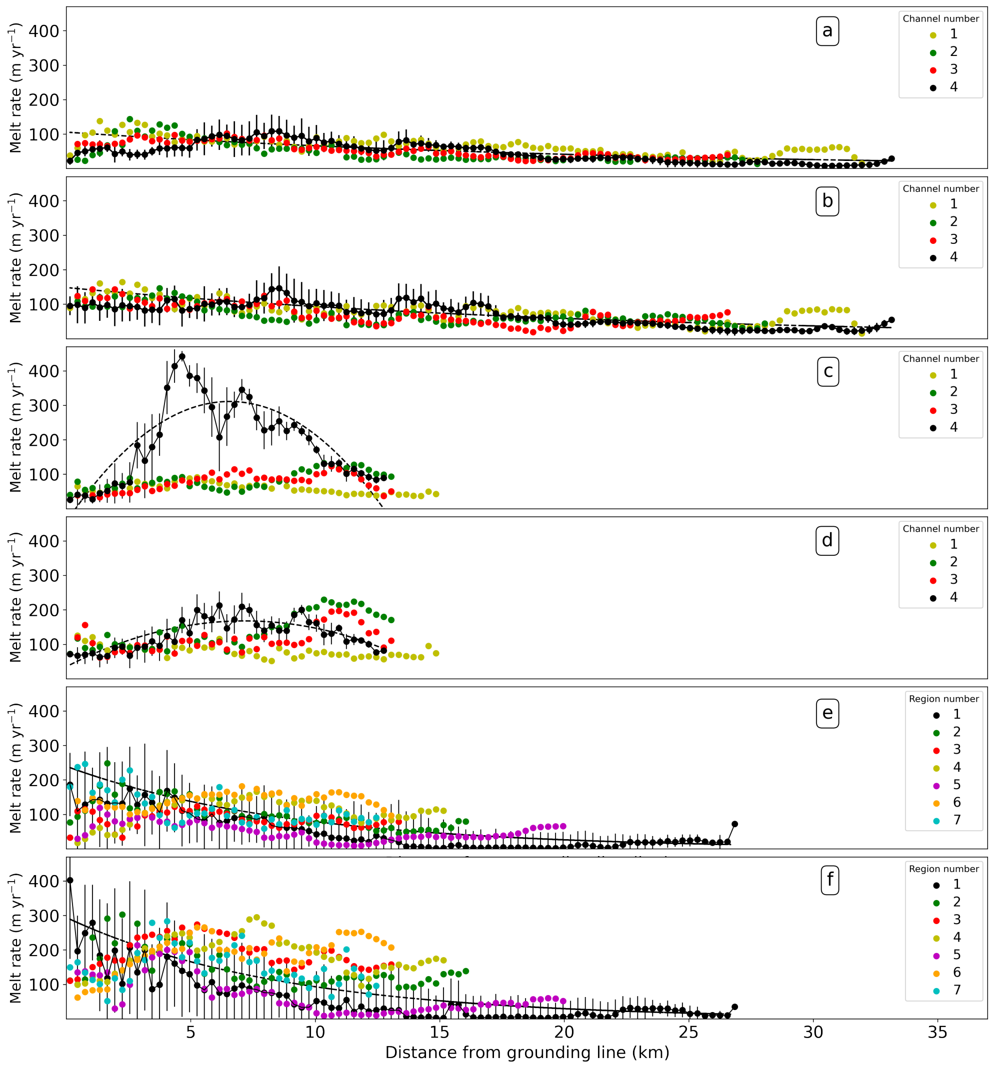

Figure 12. The basal melt rate in the *ChannelsT* experiment (without subglacial discharge) a) inside the large channels, c) inside the small channels, and e) between the channels. The basal melt rate in the *ChannelsTSubD* experiment b) inside the large channels , d) inside the small channels f) between the channels. The points represent the median melt rate in a range of 300 m. Additionally, we presented the standard deviation and a fitted curve to the melt rate for one channel and one region between the channels. See Tab. 3 for definition of experiments.

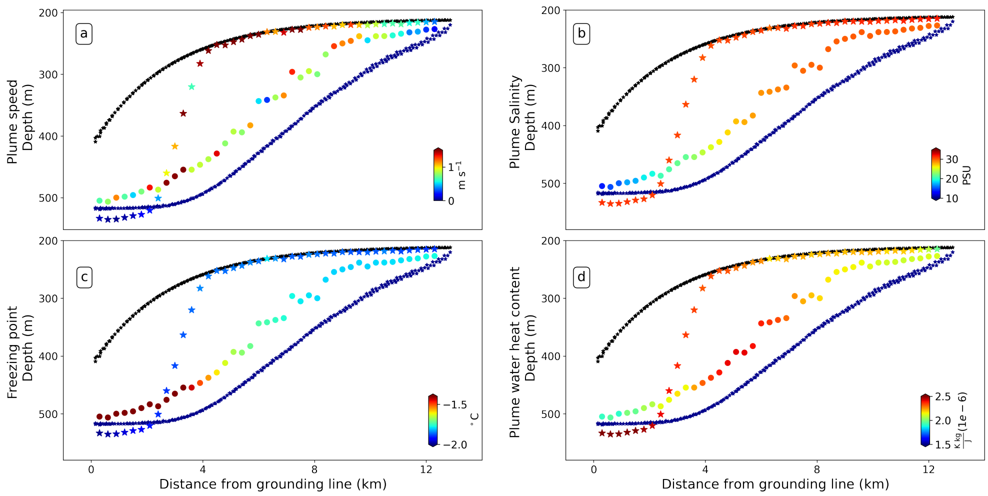

Figure 13. The plume water characteristics inside the small basal channel number 4. The black and dark blue stars (the top-most and bottom-most points) present the ice base topography inside the channel and the deepest part of the channel's walls, respectively. The colored stars and dots show the interface of the plume and ambient water in low and high subglacial discharge ($28672\,\mathrm{m^3\,s^{-1}}$) cases, respectively. The points represent the median melt rate in a range of 300 m. Note that vertically averaged equations assume the plume water is vertically mixed.